

Simultaneous Measurement of Angular and Spectral Properties of Light Scattering for Characterization of Tissue Microarchitecture and Its Alteration in Early Precancer

Young L. Kim, Yang Liu, Ramesh K. Wali, Hemant K. Roy, Michael J. Goldberg, Alexey K. Kromin, Kun Chen, and Vadim Backman

Abstract—We present a novel instrument to measure the spectral, angular, azimuthal, and polarization dependence of light backscattered by living biological tissues, thus providing the most comprehensive description of the light scattering to obtain unique quantitative information about the microarchitecture of living cells and tissues. We show the potential of this technique to characterize and diagnose early premalignant changes in the epithelia. In studies with a rodent model of colon carcinogenesis, we show that several parameters obtained using this technique, such as the number density of red blood cells in the capillary network immediately underlying the epithelium, the fractal dimension of the tissue, and the average roundness of subcellular structures, are significant for detection of precancerous changes at a very early stage of the carcinogenic process, at which no other histological or molecular markers have been identified.

Index Terms—Cancer diagnosis, fractal dimension, light scattering, Mie theory, polarization gating.

I. INTRODUCTION

STATIC elastic light scattering has been widely used to probe the structure of a variety of materials. The properties of a single light scattering depend on the structure of the scatterer and can, thus, be used to characterize the scattering object. Over the last several years, there has been a significant interest in using light scattering to probe the structure and organization of living biological tissues. These studies aim to determine the information about the sizes and refractive indices of tissue components by measuring and analyzing the backscattered light from the tissue after a single scattering event. The reasons for the growing interest in using light scattering for tissue characterization are obvious. Such techniques may provide a noninvasive means to probe tissue structure in a wide range of scales without the need for tissue removal or processing. One particularly im-

portant potential application of light scattering is the diagnosis of precancerous epithelial lesions.

More than 85% of all cancers originate in the epithelia lining the internal surfaces of the human body. The majority of such lesions are readily treatable if diagnosed at an early stage. Recent research on the molecular and cellular alterations in cancerous tissues gives us better understanding on the mechanisms of the disease. However, these advances have not translated into the diagnostic approach for early malignant lesions. Pathologists qualitatively interpret the histological characteristics such as nuclear atypia (nuclear enlargement, increased variation in nuclear size and shape, increased concentration of chromatin, roughening of the chromatin texture, the margination of nuclear chromatin, etc.) as well as architectural changes throughout the epithelium. Not only do fixation and staining limit the application of histology to study the dynamics of the disease progression in its natural environment, but also the histological image of a stained tissue sample represents the spatial distribution of the contrast dye, typically hematoxylin and eosin (H&E), which may or may not be a good representation of the actual cell structure. Therefore, some potentially important diagnostic information can be lost or altered.

Several investigators have shown that single as well as multiple light scattering can provide diagnostically valuable information about tissue structure and composition. Although the multiple light scattering and, ultimately, light diffusion inherently depend on the single light scattering by various tissue structures, the information contained in the single and multiple scattering signals is quite different. In certain cases, the use of light that has been returned from the tissue after many scattering events is advantageous. For example, this is the case when deeper tissues have to be probed. Several investigators successfully used multiple scattered light to characterize tissue structure and obtained valuable diagnostic information [1]–[8]. In many cases, the diagnostic information must be obtained from the most superficial tissue and the use of the single scattering is advantageous. This is the case when the light scattering is used to diagnose early preinvasive changes in the epithelia lining the internal surfaces of the body. It is particularly important when shallow epithelia are probed, for example, the simple columnar epithelium lining the internal surfaces of the colon. Because the dominant portion of the light returned from a tissue is scattered multiple times, distinguishing between the single and multiple

Manuscript received November 21, 2002; revised February 11, 2003. This work was supported in part by the National Cancer Foundation under Grant ACI-0219925, in part by the General Motors Cancer Research Foundation, and in part by the Phi Beta Psi Cancer Research Fund.

Y. L. Kim, Y. Liu, A. K. Kromin, K. Chen, and V. Backman are with the Biomedical Engineering Department, Northwestern University, Evanston, IL 60208 USA (e-mail: v-backman@northwestern.edu).

R. K. Wali, H. K. Roy, and M. J. Goldberg are with the Department of Gastroenterology, Evanston Hospital, Northwestern University Medical School, Evanston, IL 60201 USA.

Digital Object Identifier 10.1109/JSTQE.2003.814183

scattering components requires specialized techniques. In optical coherence tomography (OCT), an interferometer is used to isolate or gate the single scattered light reflected due to the index mismatch of internal tissue structures, when the optical path length difference between the two arms of the interferometer is within the coherence length of light source [9], [10]. The time-gating technique uses early arriving photons to eliminate the multiple scattered and diffused photons [11]–[13]. A mathematical modeling of light transport in deeper tissue layers, which describes light propagation in terms of absorption and scattering based either on diffusion, multiple-flux, or other approximations of the transport equation in the limit when the multiple scattering dominates, can be applied to account for the multiple and, particularly, diffused scattering [4], [14]. Finally, polarization gating can also be used to differentiate between the single and multiple scattering based on the fact that multiple scattering depolarizes light. In polarization gating, the tissue is illuminated by a polarized light and the returned signal is decomposed into two components with polarizations parallel and orthogonal to that of the incident light, respectively. Polarization gating has been used to probe deeper tissue layers by rejecting the scattering from the superficial tissue structures, i.e., by means of measuring the orthogonally polarized component [15], [16]. The detection of the temporal difference between the two polarized components or the detection of the perpendicularly polarized light at different wavelengths enables imaging of deep subsurface structures within highly scattering tissues [17], [18]. On the other hand, the imaging of superficially located structures of the skin, primarily within the epithelial layer, was achieved by means of measuring the degree of polarization (DOP) of the returned light, because the incident linearly polarized light was depolarized rapidly due to the multiple scattering by the birefringent collagen fibers abundant in the connective tissue underlying the epithelium [19], [20]. Moreover, the spectral analysis of the polarized component was used to obtain quantitative information about the morphology of superficial epithelial cells. For example, nuclear sizes and their average refractive index of the epithelia were determined by means of the spectral analysis of the single scattering component, minimizing the contribution of the multiple scattering by subtracting the depolarized component of the scattering signals [21]–[24].

There are two principal methods to study elastic light scattering: 1) measuring the angular and 2) the spectral distributions of the scattered light. In the first approach, the illumination wavelength is fixed and the angular distribution of the scattering light $I(\theta)$ is recorded with a goniometer [25], [26]. In the second approach, the object is illuminated by a broadband light source and the spectrum of the scattered light $I(\lambda)$ for either a specific scattering angle or integrated over a certain angular range is measured [2], [4]–[7], [14], [21]. In addition, by measuring light-scattering spectra at different scattering angles, the size distribution of particles smaller or larger than the wavelength can be obtained [23]. In this paper, we report the development of an advanced instrument, which enables measurement of both the angular and the spectral distributions of the backscattered light simultaneously. Moreover, using this technique, the azimuthal and polarization dependence of the light scattered by an arbitrary particle are obtained. We demonstrate that the measurement and analysis of this comprehensive information about

the light scattering, i.e., its spectral, angular, azimuthal, and polarization dependence, is advantageous and can be used to characterize tissue microarchitecture and its alterations associated with the initial stages of the precancerous transformations.

II. THEORETICAL AND EXPERIMENTAL MODELS

A. Theoretical Model

Light elastically scattered by a particle of an arbitrary size, shape, and internal structure can be described using the amplitude functions $S_i(\theta, \phi, \lambda)$, $i = 1, \dots, 4$, where θ is the backscattering angle (the angle between the backward direction—the direction opposite to the direction of propagation of the incident light—and the direction of propagation of the scattered light), ϕ is the azimuth of scattering, and λ is the wavelength of the incident and scattered light. These functions relate the amplitudes and phases of the incident and the scattered waves. Both waves can be represented as the linear combinations of electric vectors that are parallel E_{il} , E_{sl} and perpendicular E_{ir} , E_{sr} to the scattering plane, defined as a plane which holds the incident and the scattering rays, respectively. The scattering amplitude matrix relates these components

$$\begin{pmatrix} E_{sl} \\ E_{sr} \end{pmatrix} = \frac{e^{-i(kr - \omega t)}}{ikr} \begin{pmatrix} S_2(\theta, \phi, \lambda) & S_3(\theta, \phi, \lambda) \\ S_4(\theta, \phi, \lambda) & S_1(\theta, \phi, \lambda) \end{pmatrix} \begin{pmatrix} E_{il} \\ E_{ir} \end{pmatrix} \quad (1)$$

where k and ω are the wave vector and the angular frequency of the light, respectively, and r is the distance between the scattering particle and the point of observation. Equation (1) provides the most complete description of the scattered waves in the far-field.

The components of the scattering matrix are not completely independent. For an arbitrary particle, in the backward direction $\theta = 0^\circ$, a rotation of 180° around this axis changes the scattering matrix from $\begin{pmatrix} S_2 & S_3 \\ S_4 & S_1 \end{pmatrix}$ to $\begin{pmatrix} S_2 & -S_4 \\ -S_3 & S_1 \end{pmatrix}$. Since these two matrices must be the same, it follows that $S_3 + S_4 = 0$ for an arbitrary particle [27]. Symmetries of the scatterers can further simplify the scattering matrix. If a particle is cylindrically symmetric around the direction of propagation of the incident light, $S_3 = S_4 = 0$ and the scattering matrix is diagonal. Moreover, S_1 and S_2 are functions of the scattering angle θ only and do not depend on ϕ . A particularly important example of such symmetrical particles is a uniform sphere. Furthermore, if the scattering is observed from an ensemble of nonsymmetrical, randomly oriented particles, the averages of S_3 and S_4 are typically negligible compared to the averages of S_1 and S_2 , because the phases of S_3 and S_4 vary strongly with the orientation of the scattering particles [27], [28].

If the incident wave is linearly polarized, it is convenient to choose the laboratory system of reference such that the z -axis is along the backscattering direction and the x -axis is along the direction of polarization of the incident wave. Thus, the azimuthal angle is defined as the angle between the x -axis and the scattering plane. The scattered wave in the far-field can be represented as the superposition of two components polarized parallel (copolarized, \parallel) and perpendicular (crosspolarized, \perp) to

the polarization of the incident wave, respectively. The intensities of these two components I_{\parallel} and I_{\perp} are related to the incident intensity I_0 as

$$I_{\parallel}(\theta, \phi, \lambda) = \frac{1}{k^2 r^2} (\cos^4 \phi \cos^2 \theta |S_2^2| + \sin^4 \phi |S_1^2| - 2 \cos^2 \phi \sin^2 \phi \cos \theta \operatorname{Re}(S_1 S_2^*)) \times I_0 \quad (2a)$$

$$I_{\perp}(\theta, \phi, \lambda) = \frac{1}{k^2 r^2} \cos^2 \phi \sin^2 \phi \times (\cos^2 \theta |S_2^2| + |S_1^2| + 2 \cos \theta \operatorname{Re}(S_1 S_2^*)) \times I_0. \quad (2b)$$

If these two components I_{\parallel} and I_{\perp} are measured and the “differential polarization signal” ($\Delta I = I_{\parallel} - I_{\perp}$) is calculated at three azimuthal angles $\phi = 0^\circ, 45^\circ$, and $\phi = 90^\circ$, the amplitude functions can be calculated as

$$|S_2|^2 = \frac{k^2 r^2 \Delta I(\theta, 0^\circ, \lambda)}{I_0 \cos^2 \theta} \quad (3a)$$

$$|S_1|^2 = \frac{k^2 r^2 \Delta I(\theta, 90^\circ, \lambda)}{I_0} \quad (3b)$$

$$\cos \varphi_{12} = \frac{\Delta I(\theta, 45^\circ, \lambda)}{\sqrt{\Delta I(\theta, 0^\circ, \lambda) \Delta I(\theta, 90^\circ, \lambda)}} \quad (3c)$$

where φ_{12} is the phase difference between S_1 and S_2 (S_1 and S_2 are complex). Thus, if the intensities of polarized signals are measured for three azimuthal angles, one can reconstruct the scattering matrix and obtain the complete information about the light scattered by a symmetrical particle or an ensemble of randomly oriented nonsymmetrical particles. Furthermore, although S_3 and S_4 are not negligible compared to S_1 and S_2 , the scattering matrix can still be reconstructed. If the measurements are taken for seven different azimuthal angles, the four amplitudes $|S_i|$, $i = 1, \dots, 4$, and the phase differences φ_{12} , φ_{23} , and φ_{34} between the amplitude functions can be calculated. This underscores the importance of measuring the azimuthal dependence of light scattering, whereas in the majority of experiments and simulations, the scattered intensity is studied only as a function of either scattering angle θ or wavelength λ .

The azimuthal asymmetry of the scattering pattern, which enables the reconstruction of the scattering matrix, is a result of the polarized illumination and polarization-dependent detection. Moreover, the polarized illumination has other advantages. Most biological tissues are relatively turbid. Light propagation in such media is dominated by the multiple scattering. In order to measure the scattering matrix elements and to characterize the structure of tissue components, the single scattering signal must be decoupled from the strong signal of the multiply scattered light. As discussed above, this can be achieved by means of polarization gating [20], [21]. In this approach, the tissue is illuminated by a linearly polarized light and the copolarized (I_{\parallel}) and crosspolarized (I_{\perp}) components of the backscattered light are recorded. These components are polarized parallel and perpendicular to the polarization of the incident light, respectively. Because of the depolarization of the multiple scattered light, the contribution of the multiple scattering can be significantly reduced by subtracting off the depolarized portion of the total signal. This can be achieved by subtracting the crosspolarized

component (I_{\perp}) from the copolarized component (I_{\parallel}). The resulting differential polarization signal ($\Delta I = I_{\parallel} - I_{\perp}$) is dominated by the single scattering.

The polarized illumination and polarization-sensitive detection is advantageous over standard diffuse reflectance measurements because it enables penetration-depth selectivity. The single backscattering (ΔI) collected by means of polarization gating is primarily contributed by the scatterers located close to the tissue surface and, therefore, particularly sensitive to the properties of the superficial tissues, i.e., the epithelia. For many applications, the analysis of superficial tissues is particularly important. Early diagnosis of precancerous changes in the epithelia is an example. As discussed above, more than 85% of all cancers originate from the epithelial linings of the internal surfaces of human body. These epithelial layers can be as thin as 20 μm (one cell layer). By selecting the photons scattered within the superficial tissue layer, the properties of this scattered light can be used to characterize the structure of the epithelium and to diagnose the alterations of the epithelial microarchitecture associated with the disease. Besides the differential polarization signal (ΔI), the copolarized signal (I_{\parallel}), or the crosspolarized signal (I_{\perp}), can obtain unique depth-sensitive information. The crosspolarized signal (I_{\perp}) is primarily sensitive to the organization and composition of the deeper tissue layers, typically several millimeters below the tissue surface, rejecting the photons backscattered in the superficial tissues [16]. The analysis of this component is advantageous for a variety of applications, if it is necessary to probe a tissue structure deep below the surface. The copolarized signal (I_{\parallel}) has, on average, a more shallow penetration than the crosspolarized signal (I_{\perp}). Combinations of these two components such as the total signal ($I_{\parallel} + I_{\perp}$) and the DOP ($|I_{\parallel} - I_{\perp}|/|I_{\parallel} + I_{\perp}|$) can be obtained as well.

B. Animal Cancer Model

To show the feasibility of using the information provided by the spectral-angular maps to study the initial stages of carcinogenesis, we conducted studies involving an animal model of colon cancer, i.e., Fisher rats treated with azoxymethane (AOM), which is a colon-specific carcinogen. The AOM animal model has been the most widely used animal model over the last decade for studying colon carcinogenesis and chemopreventive agents [29], [30]. Several ongoing nutritional and chemopreventive trials in human colon cancer are, in part, based on the results generated using the AOM model. To date, no “side effects” of AOM that are not directly related to carcinogenesis have been established. The AOM model is the most robust animal model because of the strong similarities in the morphological, genetic, and epigenetic alterations with human colon carcinogenesis [31]. The same molecular and biochemical markers such as K-ras, AKT, β -catenin, PKC, MAP kinase, and aberrant crypt foci (ACF) in human cancer are identically activated in the AOM model. For example, ACF are precursor lesions, which are observed on the colonic mucosal surface of the AOM model and human cancer [30]. ACF, the earliest detectable biomarker to colon carcinogenesis, develop within 5–10 weeks after AOM injection. A small proportion of ACF develop dysplasia, evolve into adenomas, and some adenomas eventually degenerate into carcinomas. Adenomas

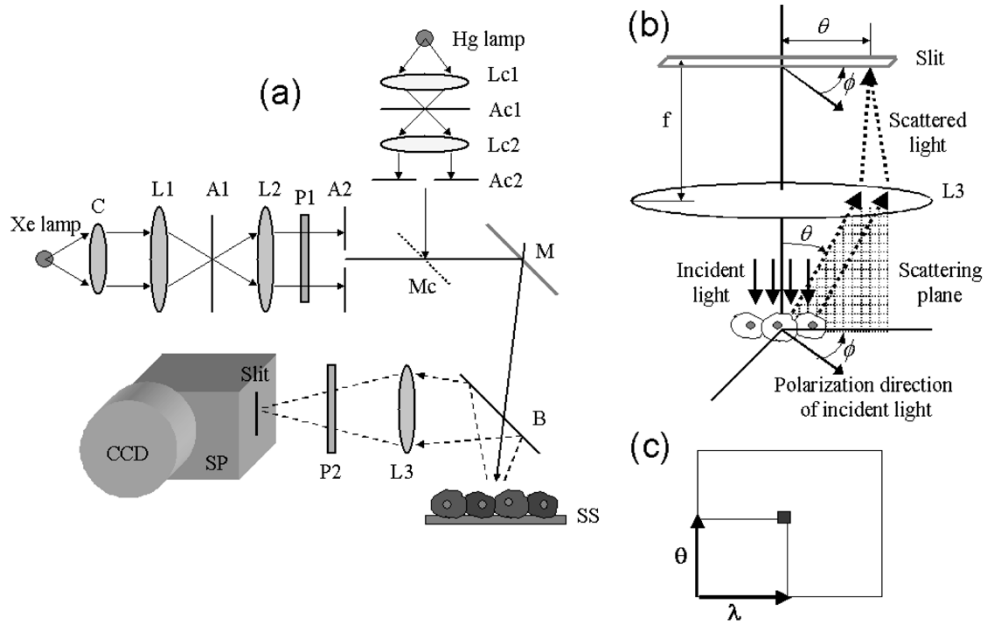


Fig. 1. Schematic diagram. (a) C: condenser, L1 L2: collimating lenses for xenon arc lamp, A1 A2: apertures, P1 P2: polarizers, M: mirror, B: beam splitter, SS: sample stage, L3: collecting lens, SP: spectrograph, and Lc1 Lc2 Ac1 Ac2 Mc: components for spectrograph calibration. (b) Unfolded view without the polarizer P2 and the beam splitter B. The azimuthal angle ϕ is defined by the polarization direction of the incident light and the entrance slit of the spectrograph. The entrance slit was at a focal distance from the lens L3. All scattered rays with an identical scattering angle θ and an azimuthal angle ϕ are focused into a point on the entrance slit. (c) The spectrograph spreads the light in the direction perpendicular to the slit according to its wavelengths. Thus, the CCD records a matrix $I(\lambda, \theta)$ of the scattered intensities.

and adenocarcinomas typically are detectable 20–30 weeks after the AOM injection. Both the ACF and tumors show distal colon predominance, further mirroring human sporadic colon cancers. An increased blood supply due to neovascularization (i.e., angiogenesis) of mucosal and submucosal tissues is observed approximately 40 weeks after AOM administration. At a genetic level, AOM leads to the production of O^6 -methyl-guanine residues in the DNA resulting in mutations of a variety of genes, including β -catenin and K-ras, and overexpression of AKT and epidermal growth factor receptor activation. Recent reports have suggested that some genetic events may precede the development of ACF. The cellular correlates of genetic and epigenetic changes include inhibition of apoptosis, allowing the otherwise short-lived colonocytes to accumulate requisite mutations for neoplastic transformation and increased proliferation, allowing clonal expansion of initiated cells. It must be emphasized that these critical initial cellular and genetic events have no currently identifiable morphological correlates; thus, with the current armamentarium, these lesions are impossible to diagnose. The development of technologies to detect these lesions would be of considerable clinical importance given the “field effect” of colon carcinogenesis. Thus, assessment of early lesions in the distal, more accessible colon, may provide accurate risk-stratification for more invasive procedures. For the animal part of these experiments, we, therefore, wanted to focus on time-points during carcinogenesis where no current biomarkers are available.

III. MATERIALS AND METHODS

A. Experimental Setup

In order to obtain the most comprehensive information about the spectral, angular, azimuthal, and polarization dependence

of light scattering, we have developed a novel instrument [Fig. 1(a)]. A broadband light from a 75 W Xenon arc lamp (Oriel, Inc., Stratford, CT) was collimated by a condenser C ($f/1$, two element fused silica, Oriel, Inc., CT) and a 4-f relay system consisted of lenses L1 (achromat, $f = 160$ mm, $D = 40$ mm, Melles Griot, Irvine, CA), L2 (achromat, $f = 300$ mm, $D = 50$ mm, Melles Griot, CA), and an aperture A1. The resulting beam had a divergence of 0.2° . This beam was polarized by a polarizer P1 (Dichroic sheet polarizer, Melles Griot, CA) and its diameter was reduced to 1 mm by a field diaphragm A2. A mirror M deflected the beam through the beamsplitter (broadband nonpolarizing, Newport, CA) onto the sample, which was mounted on a sample stage SS. To avoid the specular reflection from tissue surface, the incident beam was orientated at an angle of 15° to the normal to the sample surface. The light scattered by the sample was collected by means of a lens L3 ($f = 31$ mm, $D = 17.5$ mm, Melles Griot, CA). A polarizer P2 selected the polarization state of the scattered light so that the copolarized component (\parallel) and the crosspolarized component (\perp) of the scattered light could be recorded independently. The entrance slit of a spectrograph SP (SpectraPro-150, Acton Research Corp., Acton, MA) was placed in the focal plane of the lens L3. This spectrograph was coupled with a charge-coupled device (CCD) camera (CoolSnapHQ, Roper Scientific Inc., Trenton, NJ). The spectrograph was positioned such that its entrance slit was at a focal distance from the lens L3. Therefore, all scattered rays with an identical scattering angle θ and an azimuthal angle ϕ were focused into a point on the entrance slit as shown in Fig. 1(b). An angular distribution of the scattered light was projected onto the slit of the spectrograph. For example, the scattering in the backward direction was mapped at the center of the slit. The azimuthal angle ϕ was defined by the

angle between the direction of the spectrograph slit and the polarization direction of the incident beam, which was selected by rotating the polarizer P1. The copolarized intensity (I_{\parallel}) and the crosspolarized intensity (I_{\perp}) were measured by rotating the polarizer P2 parallel and perpendicular to the polarizer P1, respectively. The spectrograph spread the light in the direction perpendicular to the slit according to its wavelengths. Thus, the CCD recorded a matrix of the scattered intensities, where one axis corresponded to the wavelength of light λ and the other to the angle of scattering θ for a fixed azimuthal angle ϕ and a polarization state as shown in Fig. 1(c). These maps were collected for three azimuthal angles, $\phi = 0^\circ$, 45° , and 90° , in the spectral range from 400 to 700 nm, and for the scattering angles θ ranging from 0° to 12° . After the copolarized intensity maps $I_{\parallel}(\lambda, \theta)$ and the crosspolarized intensity maps $I_{\perp}(\lambda, \theta)$ were collected for $\phi = 0^\circ$, 45° , and 90° , the sample was removed and the background intensities were measured for each ϕ and subtracted from I_{\parallel} and I_{\perp} to remove stray illumination component and the background noise. Hereafter, I_{\parallel} and I_{\perp} refer to the intensity maps after the background subtraction. These maps were normalized by the respective intensity maps I_{\parallel}^{xe} and I_{\perp}^{xe} collected from a reflectance standard (Ocean Optics, Inc., Dunedin, FL) to account for the nonuniform spectrum of the xenon lamp illumination and other artifacts. Then, the differential polarization intensity maps were calculated as $\Delta I = I_{\parallel}/I_{\parallel}^{xe} - I_{\perp}/I_{\perp}^{xe}$. For spectrograph calibration, a mercury lamp (Ocean Optics, Inc., FL) was used. The calibration beam was collimated and impinged upon a mirror Mc, which was mounted on a flipper (New Focus, San Jose, CA). Depending on the orientation of the flipper, either the xenon or the mercury light beams reached the sample stage. The calibration beam was reflected by the reflectance standard and collected by the spectrograph. Thus, the position of the spectrograph grating was calibrated with the emission lines of the mercury lamp.

B. Tissue Phantoms

The instrument was tested and calibrated with tissue phantom consisting of the aqueous suspensions of polystyrene microspheres (refractive index $n = 1.59$) (Polyscience, Inc., Warrington, PA) of various diameters ranging from $1 \mu\text{m}$ to $10 \mu\text{m}$. The first purpose of these experiments was to study the efficacy of the polarization gating for the decoupling of the single and multiple scattering components of the returned signal. The number density of the microspheres was increased and the scattering coefficient μ_s was calculated using Mie theory. The optical thickness τ of the tissue phantom was varied from 0 to 5.5 ($\tau = \mu_s z$, where z is the physical depth of the medium; light traversing a medium with $\tau = 1$ undergoes, on average, one scattering). The copolarized signal (I_{\parallel}) and the crosspolarized signal (I_{\perp}) were recorded at the three azimuthal angles and the differential polarization intensity (ΔI) was calculated by subtracting I_{\perp} from I_{\parallel} . Also, the DOP, defined as $\text{DOP} = (|I_{\parallel} - I_{\perp}|/|I_{\parallel} + I_{\perp}|)$, was calculated from the same data. The second purpose of these experiments was to ensure the proper calibration of the instrument. To achieve this, we compared the angular, azimuthal, and spectral distributions of the scattered signals with those simulated using Mie theory. The

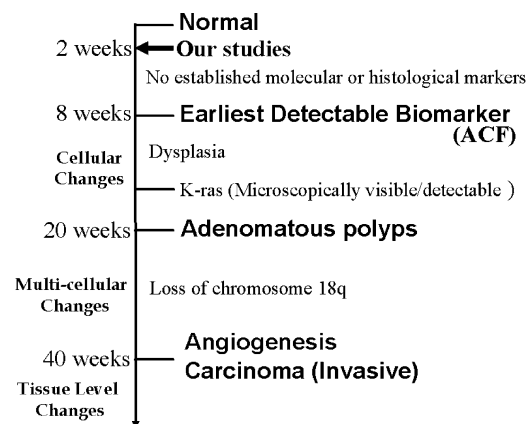


Fig. 2. Development process of rat-carcinogenesis model.

spectral distributions at several fixed scattering angles and the angular distributions at several fixed wavelengths were compared with Mie theory for all azimuthal angles.

C. Animal Protocols

Six male Fisher 344 rats, initially weighing 80–100 g, were divided into two equal groups. The rats in the first group were injected weekly (for two weeks) with AOM (20 mg/Kg body weight) and the rats in the second (control) group were injected with saline only. The rats were sacrificed after two weeks of the second AOM/saline injections. The colons were removed, flushed with phosphate-buffered saline and opened up longitudinally. Segments of the colons were spread on a glass slide. The light scattering data were collected from 20 sites (most of them were collected from distal segments, where the majority of precancerous and cancerous lesions are expected to develop at a later stages of the carcinogenic process). For each site, the data were collected simultaneously from approximately 1000 cells. The spectral and angular distributions as well as the azimuthal dependence were analyzed to calculate the number density of red blood cells (RBCs) in the capillary network underlying the epithelium, the fractal dimension of tissue microarchitecture, and the average roundness of subcellular structures. After collecting the scattering data, the colon segments were methylene blue stained (0.02%) and subjected to microscopic identification of ACF [32]. At this early stage, no ACFs or other neoplastic lesions were detected in the colons of the AOM-treated rats. ACFs are the first histologically apparent changes that form only after 5–10 weeks following the AOM injection. Adenomas will start to occur approximately 20 weeks from the injection, whereas angiogenesis and carcinomas take about 40 weeks to develop. Thus, we analyzed the tissues at very early stages of the neoplastic (preinvasive) disease. Specimens from these colons, fixed in 10% buffered formaline, were submitted to pathology to obtain the histological sections of the colon tissues. Fig. 3 shows two horizontal sections through several crypts from the control and AOM-treated colon tissues. The majority of cells in the crypts are columnar cells, which are the principal cell type in the epithelium of the colonic mucosa. We point out that, at this early stage, no morphological changes of a stained mucosa can be detected by means of microscopic examination. (See Fig. 2 for overall time course and development process.)

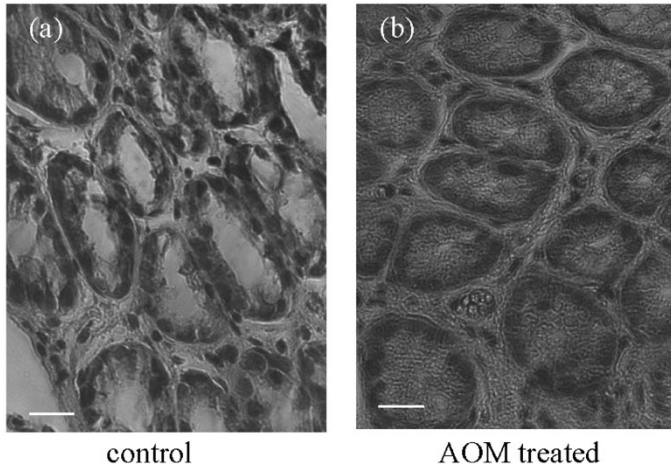


Fig. 3. Microscopic sections of control and AOM-treated rats. (a) and (b) are the horizontal sections through several crypts of the control and AOM-treated colons, respectively. The scale bars are $30 \mu\text{m}$.

IV. RESULTS

A. Polarization Gating

As discussed in the Materials and Methods section, we conducted experiments with tissue phantoms to investigate the efficacy of the polarization gating to decouple the single and multiple scattering components in the returned signal. In these experiments, we consequently varied the optical thickness τ of the tissue phantoms and recorded the wavelength-scattering angle maps of the copolarized and crosspolarized scattering signals. We demonstrated that the single scattering component can be restored by means of the polarization gating for all angles of collection achieved with this instrument as shown in Fig. 4(a). After the depolarized signal is subtracted, the differential polarization signal ($\Delta I = I_{\parallel} - I_{\perp}$) first increases and then saturates with τ as $\Delta I(\tau) = 1 - e^{-\alpha\tau}$, with $\alpha = 1.41$. Fig. 4(b) shows the rate of the increase in the differential polarization signal with the optical thickness, representing the contribution of different layers to the differential polarization signal. The contribution from a tissue layer at optical thickness τ decreases with τ as $e^{-\alpha\tau}$. Approximately 98% of the signal is contributed by the superficial layer within $0 \leq \tau \leq 2$. After the optical thickness $\tau = 2$, the contribution is negligible compared with the optical thickness $\tau \leq 2$. Therefore, the subtraction of the crosspolarized signal (I_{\perp}) from the copolarized signal (I_{\parallel}) effectively selects the photons that return from the tissue after only a single scattering on average. These experiments demonstrate that the polarization gating is capable of substantially reducing the effect of multiple scattering. When polarization gating is used to study living tissues, the majority of the differential polarization signal is contributed by the superficial tissue layer, mostly, the epithelia with the optical thickness $\tau \leq 2$. Since the scattering coefficient μ_s depends on the tissue composition, organization, and structure, the physical thickness (i.e., the depth of measurements) may vary for different tissue types. Our studies with rat colonic mucosal tissues indicate that the polarization gating selects the photons that are scattered within the superficial tissue layers approximately $30\text{--}40 \mu\text{m}$ deep. Because the colonic mucosa is lined with a single layer of columnar epithelial cells,

which are about $20 \mu\text{m}$ tall, histologically, the first $30\text{--}40 \mu\text{m}$ into the colonic tissue corresponds to the epithelial layer and the uppermost portion of the underlying connective tissue layer (lamina propria) which contains the networks of extracellular matrix and capillaries supporting the epithelium and providing it with the blood supply. For comparison, Fig. 4(c) shows the DOP calculated from the same data. DOP is maintained even for large values of the optical thickness. For example, 50% of DOP is preserved for $\tau = 4$, showing that the copolarized signal (I_{\parallel}) alone cannot eliminate the multiple scattering as effectively as the differential polarization signal (ΔI).

B. Multidimensional Scattering Intensity Maps

Figs. 5 (a)–(c) and 6 (a)–(c) show the spectral-angular images of the differential polarization signals for the three azimuthal angles collected in the experiments with the aqueous solutions of the polystyrene microspheres of two different sizes. Fig. 5 shows the images collected from the suspension of microspheres distributed in size with the mean diameter of $5.80 \mu\text{m}$ and a standard deviation of $0.019 \mu\text{m}$. Fig. 6 shows similar images obtained for larger microspheres with a mean diameter of $9.80 \mu\text{m}$ and a standard deviation of $0.30 \mu\text{m}$. These maps show the intensity distributions as a function of both backscattering angle θ and wavelength λ . For comparison, in each figure, the images (d)–(f) were simulated using Mie theory for the same size distributions and refractive index. All of the experimental maps are in good agreement with the simulations for all three azimuthal angles. Fig. 5 shows the symmetric patterns, with respect to the backward direction ($\theta = 0^\circ$), over the scattering angle θ from -5° to 5° . We took advantage of this symmetry by imaging half of the angular distribution and reducing the distance between the sample and the collecting lens L3, thus increasing the angular range up to 12° . Fig. 6 shows the spectral-angular maps of the backward scattering by the $9.30\text{-}\mu\text{m}$ polystyrene microspheres (left panels) and the corresponding Mie simulations for the three azimuthal angles (right panels). As in the experiment with the $5.80\text{-}\mu\text{m}$ microspheres, a good agreement between the theory and the experiments was achieved. The spectral-angular maps reveal several important characteristic features of the large particle scattering. 1) The ripple structures, high-frequency oscillation patterns, arising from the interference of the backscattered light, are apparent. Since the ripple structures are periodic in inverse wavelength, the width of the ripple structures become larger as the wavelength increases as shown in Fig. 7(a). 2) The scattering patterns show different lobes in the angular distribution, which vary with the particle size. The angular distribution of the smaller particles is more uniform than that of the large particles as shown in Fig. 7(b). The distance between two neighboring lobes (e.g., the central lobe and the next lobe) becomes larger with the wavelength. 3) The azimuthal dependence is obvious for the larger particles as shown in Fig. 6. The strongest intensity is observed in the backward direction ($\theta = 0^\circ$) for $\phi = 0^\circ$ and in the near backward direction ($\theta = 2^\circ \sim 3^\circ$) for $\phi = 90^\circ$. For $\phi = 45^\circ$, the intensity pattern is more uniform over all scattering angles. The scattering intensities in the backward direction $\theta = 0^\circ$ are the same for all three azimuthal angles because the particles are spherical. 4) The spectral-angular

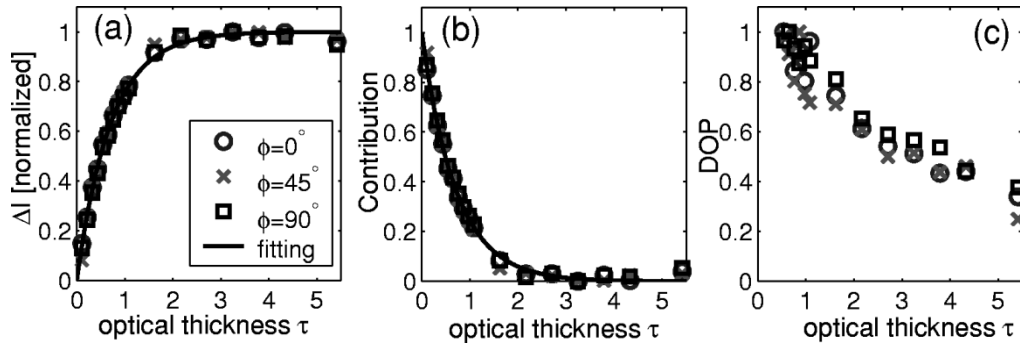


Fig. 4. (a) Differential polarization signal ($\Delta I = I_{\parallel} - I_{\perp}$) for the tissue phantoms averaged for 400–700 nm as the optical thickness increases. 98% of the signal is contributed within the superficial layers of the tissue phantom ($0 \leq \tau \leq 2$). The fitting curve is $\Delta I(\tau) = 1 - e^{-\alpha\tau}$, with $\alpha = 1.41$. (b) The rate of the increase in ΔI . The contribution from different layers at optical thickness τ to $\Delta I(\tau)$ decreases with τ as $e^{-\alpha\tau}$. After $\tau = 2$, the contribution is negligible. (c) $\text{DOP} = (|I_{\parallel} - I_{\perp}| / (|I_{\parallel} + I_{\perp}|))$, calculated from the same data, decreases with τ but the partial DOP is maintained for large values of the optical thickness.

maps of the smaller particles ($5.80 \mu\text{m}$) show less azimuthal asymmetry than those of the larger particles ($9.30 \mu\text{m}$).

C. Alterations of Tissue Microarchitectures in Early Carcinogenesis

We conducted pilot animal studies with AOM-treated Fisher rats to show the feasibility of using the information provided by the spectral-angular maps to characterize tissue microarchitecture and to investigate its alterations in the initial stages of carcinogenesis. In these experiments, we compared the light-scattering properties of control and precancerous rat colonic tissues. The carcinogen-rats and the control rats were injected with AOM and saline, respectively. The data were collected after two weeks of AOM administration, at which time, there are no conventionally detectable morphological alterations. We found significant differences between the differential polarization signals (ΔI) of the control and AOM-treated tissues in the distal colons but not proximal colon as shown in Fig. 8 between (a) and (b) and (c) and (d). This data is consonant with the predilection of AOM for the distal colon and underscores the biological significance of these findings. Furthermore, the similarity of the images from the proximal colon between the control and treated rats emphasizes the interanimal reproducibility of these measurements.

Fig. 9(a) shows the typical spectral distribution averaged over θ from $\theta = -2^\circ$ to $\theta = 2^\circ$ for the control and AOM-treated tissues, respectively. The spectra of the differential polarization signals obtained from the control colons do not exhibit characteristic hemoglobin (Hb) absorption bands at 542 and 577 nm. Hb is the only significant absorber of the visible light in colonic and many other tissues. Because RBCs are located below the epithelium, the absence of the Hb absorption bands in the spectra of the control colonic tissues indicates that, in these measurements, the epithelia (about a $20\text{-}\mu\text{m}$ -thick one cell layer) gave rise to the majority of the differential polarization signal ($\Delta I = I_{\parallel} - I_{\perp}$). However, the spectra obtained from the AOM-treated distal colons show certain degree of Hb absorption, thus indicating that RBCs were present in the tissue immediately below the epithelium. This finding has two implications on the analysis of the differential polarization signals. 1) In order to analyze pure scattering signals unaffected by the Hb absorption to investigate the microarchitecture of the epithe-

lial tissues, the effect of Hb must be removed. As discussed, we show that by removing RBC contribution to differential polarization signals, endogenous properties of epithelial cells, such as their mass density correlation function [Figs. 10 and 11(c)], and the roundness of intracellular structures [Fig. 11(d)] can be assessed and used to accurately diagnose the earliest stages of precancer. 2) The concentration of Hb and the number density of RBCs can be estimated from these measurements, which may provide useful diagnostic and physiological information. Both objectives can be easily achieved, if the spectral-angular images of isolated RBCs can be separately measured.

We used the differential polarization signals ($\Delta I = I_{\parallel} - I_{\perp}$) to measure the number density of RBCs near the tissue surfaces. To separate the contribution from the scattering and absorption in the differential polarization signals, we obtained the scattering images of rat RBCs. Although Hb primarily absorbs visible light, it is not sufficient to measure only the absorption spectra of the Hb molecules. RBCs, which are filled with Hb, are large scatterers, approximately $7\text{--}8 \mu\text{m}$ in diameter. Therefore, the contribution from the RBCs couples both absorption and scattering. First, blood samples were taken from the control and AOM-treated Fisher rats. Each blood sample was smeared out on a glass slide and the spectral-angular maps were recorded as discussed above [Fig. 9(b)]. We found that the blood samples from both AOM-treated and control rats were identical. Immediately after the measurements, the number of RBCs per unit area (square millimeter) was counted with a conventional microscope. Based on the signal level of RBCs ($\Delta I_{\text{RBC}}(\lambda)$) measured with our instrument and the number of RBCs per unit area (Ω) counted with a microscope, the differential polarization signal after subtracting the Hb absorption $\Delta I_F(\lambda)$ is given by

$$\Delta I_F(\lambda) = \Delta I_{\text{TIS}}(\lambda) - \alpha \frac{\Delta I_{\text{RBC}}(\lambda)}{\Omega} \quad (4)$$

where $\Delta I_{\text{TIS}}(\lambda)$ is the original signal collected from the colon tissue, $\Delta I_{\text{RBC}}(\lambda)$ is the RBC signal collected from the blood sample, and α is the number density parameter (the number of RBCs per square millimeter). If the RBCs' scattering is properly subtracted, the resulting spectrum should not exhibit Hb absorption bands. We have developed an algorithm to find the fitting parameter α by minimizing the Hb absorption bands in ΔI_F

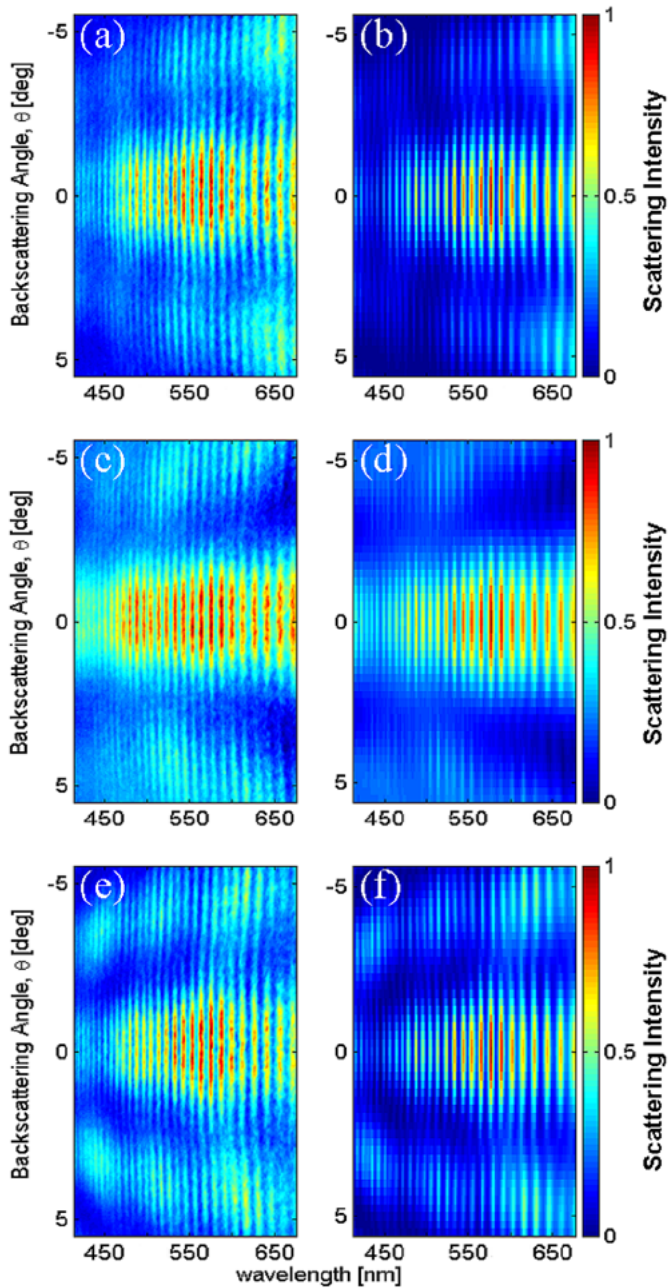


Fig. 5. Spectral-angular intensity images ($\Delta I(\lambda, \theta)$) of the light scattered by the aqueous suspension of microspheres distributed in size with the mean diameter of $5.80 \mu\text{m}$ and the standard deviation of $0.019 \mu\text{m}$. The data were collected in the single scattering regime with the optical thickness of the phantom $\tau = 3$. (a), (c), and (e) (panels on the left) are the experimental data. (b), (d), and (f) (panels on the right) are the images simulated using Mie theory. (a) and (b): $\phi = 0^\circ$, (c) and (d): $\phi = 45^\circ$, (e) and (f): $\phi = 90^\circ$.

[Fig. 9(c)]. Fig. 9(d) shows that after RBC contribution subtraction, the spectra from the AOM-treated distal colons do not exhibit the signatures of Hb absorption. Such spectra are the scattering fingerprints of the tissue microarchitecture. Importantly, the spectra of the AOM-treated colons and the control colons are distinctly different. Thus, the spectral differences in the distal colons are not due to the Hb absorption alone but show the existence of certain structural differences between the normal and precancerous epithelia. Fig. 11(a) compares the number density of RBCs (per unit area) obtained from the light scattering data

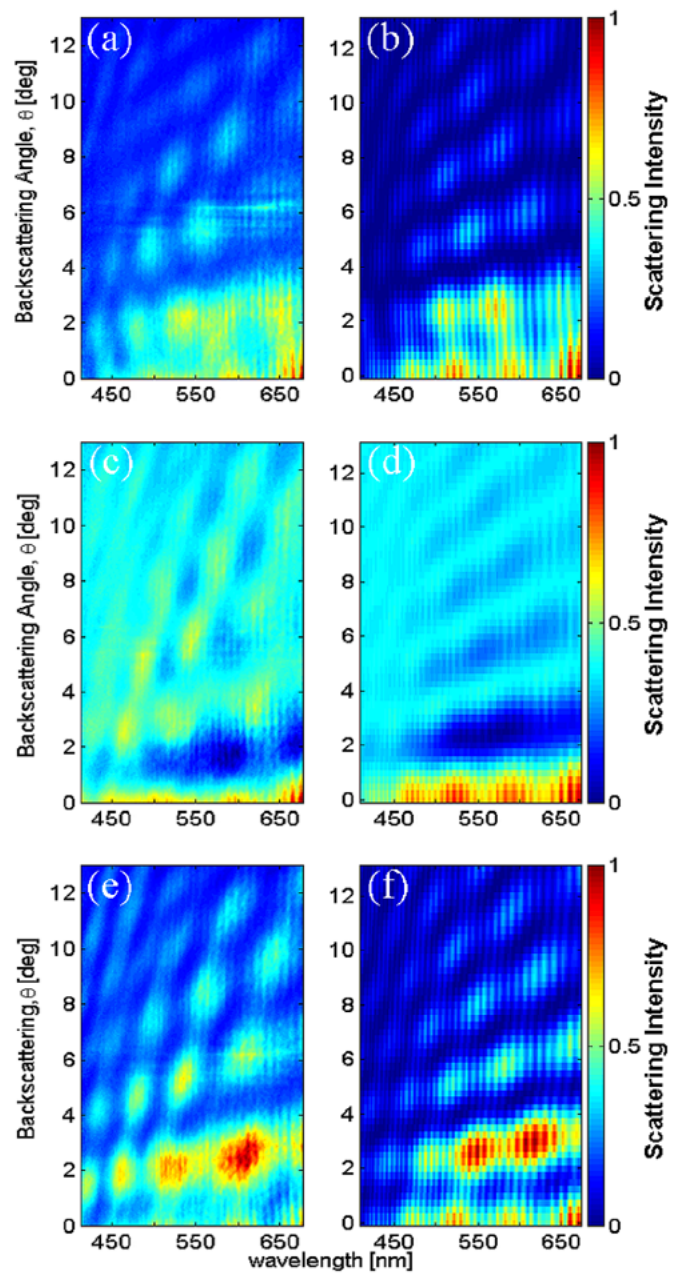


Fig. 6. Spectral-angular intensity images ($\Delta I(\lambda, \theta)$) of the light scattered by the aqueous suspension of microspheres distributed in size with the mean diameter of $9.30 \mu\text{m}$ and the standard deviation of $0.03 \mu\text{m}$. The data were collected in the single scattering regime with the optical thickness of the phantom $\tau = 3$. (a), (c), and (e) (panels on the left) are the experimental data. (b), (d), and (f) (panels on the right) are the images simulated using Mie theory. (a) and (b): $\phi = 0^\circ$, (c) and (d): $\phi = 45^\circ$, (e) and (f): $\phi = 90^\circ$.

for the control and AOM-treated distal colons. The precancerous tissues exhibit several-fold increase in concentration of RBCs in the near-epithelial capillary network. The P-value (one-tailed) was found to be 0.0002. Because the differential polarization signal (ΔI) is the most sensitive to the single scattering events immediately below the epithelia, we conclude that the increase in blood supply did not originate from deeper mucosal and sub-mucosal tissues but rather from the capillary network immediately underlying the epithelia.

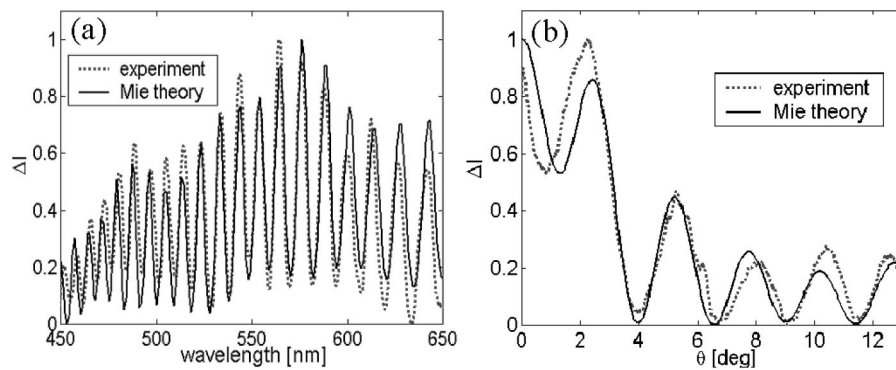


Fig. 7. Cross sections of angular-spectral images. (a) The horizontal cross section of Fig. 5(a) at $\theta = 0^\circ$. (b) The vertical cross section of Fig. 6(a) at $\lambda = 540 \text{ nm}$ and $\phi = 0^\circ$. The dotted lines are the experimental data and the solid lines are the Mie simulations, respectively.

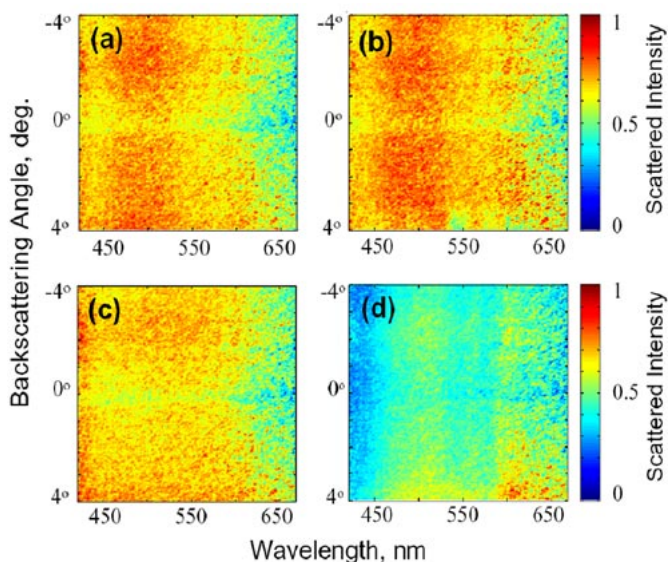


Fig. 8. Spectral-angular images of preinvasive rat colon cells. The images show the intensity of the light scattering signal for various wavelengths and angles of backscattering at $\phi = 0^\circ$. (a) Control rat, proximal colon, (b) AOM-treated rat, proximal colon, (c) control rat, distal colon, and (d) AOM-treated rat, distal colon. The spectral-angular images for proximal colons are similar and the images for distal colons are distinctly different.

Many investigations have been performed to study increased blood supply to precancerous lesions at more advanced stages of the disease, which is usually due to the angiogenesis in the mucosal and submucosal tissues [33]. Because the process occurs throughout the mucosa and submucosa, typically several millimeters from tissue surface, these changes can be detected using diffuse reflectance measurements. In such measurements, diffuse reflectance signal is collected and its spectrum is analyzed to determine the Hb concentration averaged over relatively large volumes of the tissue, typically several cubic millimeters. We have investigated the alterations of Hb concentration in deeper tissues by means of the analysis of the crosspolarized signal (I_{\perp}) using a conventional algorithm [4]. Fig. 11(b) shows that the Hb concentration in deeper tissues is not statistically different between the AOM-treated and control rats (P-value = 0.072). Compared with the dramatic five-fold increase in the blood supply near the epithelia [Fig. 11(a)], the Hb concentration in deeper tissues does not exhibit a significant increase in the AOM-treated rats. This result indicates that in the initial stages of carcinogenesis the blood supply increases only

in the immediate vicinity of the epithelia in the AOM-treated rats. Future investigations are needed to determine the precise biological mechanism of this effect. We note that the increased blood supply has not been previously documented in the initial stage of the precancerous transformations and is believed to occur only at a later stage of the disease (i.e., in AOM-treated rat model the angiogenesis is typically observed in approximately 40 weeks after AOM administration).

The angular distributions of the scattered light were used to calculate the fractal dimensions of tissue microarchitecture. Several investigators have shown that many biological tissues have fractal-like organization and are statistically self-similar [34]–[36]. There is a developing interest in investigating the fractality of tissues. Traditionally, light scattering has been used to study fractality of aggregated particles [37]. The dependence of the scattering intensity on the scattering angle θ can provide information about the fractal dimensions of biological tissues at subcellular and multicellular scales [38]. Since the fractal dimension is related to the mass density correlation function $C(r) = \langle \rho(r')\rho(r'+r) \rangle$, where $\rho(r)$ is a local mass density at r , it quantifies how well the tissue structures separated by various distances are correlated and how compact the tissue is. For example, the mass fractal dimension of an object with uniform density distribution equals 3, the same as the Euclidean dimension of the underlying space. The mass density correlation function $C(r)$ and the scattering intensity $\Delta I(\theta)$ are related by means of the Fourier transform [38]. Because the correlation function $C(r)$ is proportional to r^{D-3} , where D is the mass fractal dimension, D can be obtained from the angular distribution of the light scattering [37]. The angular distribution $\Delta I(\theta)$ at 500 nm of the AOM-treated and control colon tissues were Fourier transformed and the slopes of their power spectra in the linear regions of the log-log scale were calculated. Because the value of a slope is $D - 3$, the mass fractal dimension was determined for each tissue site as shown in Fig. 10, which also shows a fractal nature in the tissue microarchitectures because the mass correlations function $C(r)$ is described by the power law (r^{D-3}) in linear scale. Fig. 11(c) shows that, on average, the fractal dimensions of the control colon tissues are higher than those of the AOM-treated colon tissues with one-tailed P-value = 0.033. This indicates that the mass density autocorrelation function $C(r)$ of AOM-treated colon tissues is steeper and decreases faster with the separation

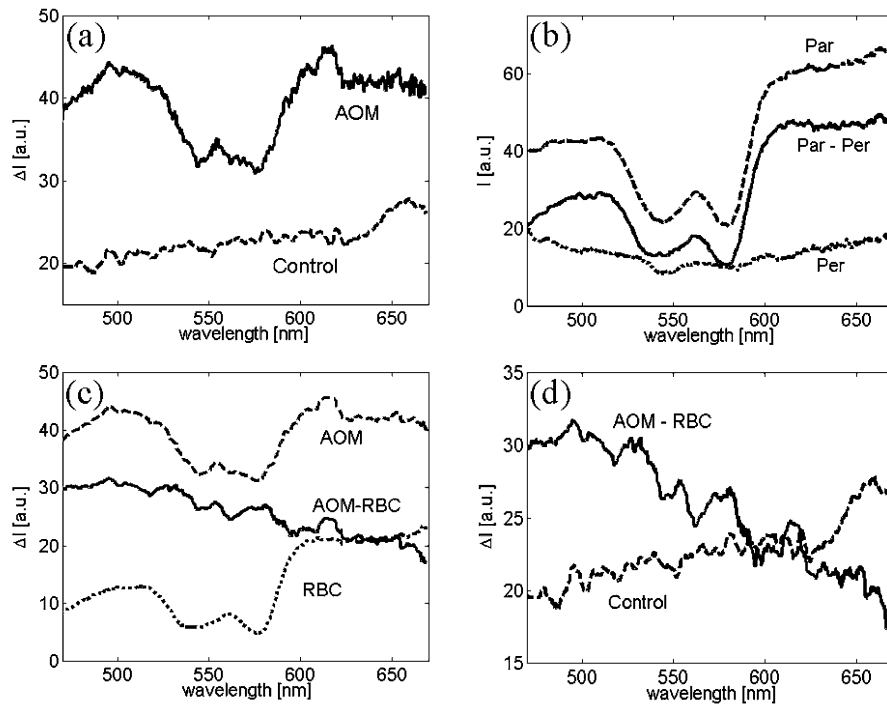


Fig. 9. Spectral analysis. (a) The spectra of control and AOM-treated colon tissues at $\theta = 0^\circ$. (b) The spectrum of RBCs, where Par, Per, and Par-Per represent I_{\parallel} , I_{\perp} , and $\Delta I = I_{\parallel} - I_{\perp}$, respectively. (c) Subtraction of RBC contribution from the spectrum of a distal colon of an AOM-treated rat. (AOM: original tissue spectrum, RBC: spectrum from a suspension of RBCs, and AOM-RBC: tissue spectrum after the RBC signal subtraction.) (d) Comparison of the spectra of the distal colon tissues from of the control and AOM-treated rats after the RBC subtraction. The spectral differences are due to internal structures in the epithelia and not due to the difference in RBC contribution.

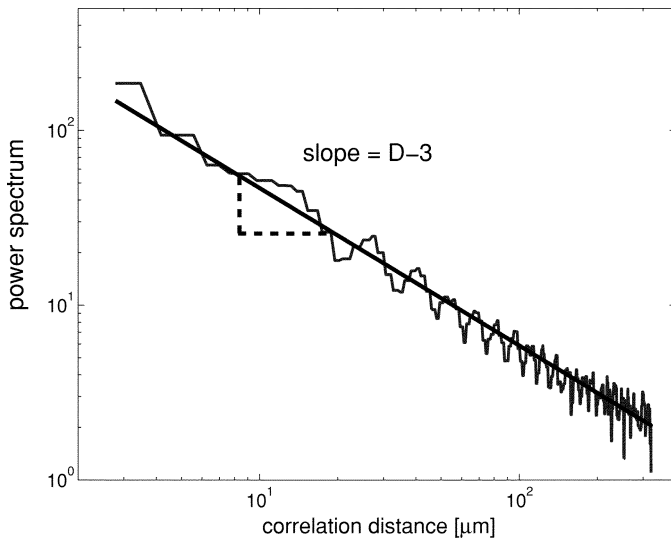


Fig. 10. Power spectrum of the angular distribution. The power spectrum is proportional to the mass density correlation function $C(r)$, where r is the length scale of the mass density correlation. The black line is the best fit by a power law ($C(r) \sim r^{D-3}$), showing the self-similar nature of microarchitecture of the epithelium. The slope is $D - 3$, where D is the fractional dimension.

between two points. This, in turn, shows that the organization of the AOM-treated tissues may be altered even at the earliest stages of the disease.

The azimuthal dependence of the scattered light offers a tool to measure the average roundness of particles. For uniform sphere particles, $|S_2|^2/|S_1|^2$ equals 1 in the backward direction ($\theta = 0^\circ$) [27]. It was also shown that the ratio of $|S_2|^2$ to $|S_1|^2$ highly correlates with the average roundness of particles [39].

Thus, if the average shape of scattering particles is nonspherical, the average roundness ratio $R = |S_2|^2/|S_1|^2$ deviates from the unity. Since both $|S_2|^2$ and $|S_1|^2$ can be obtained from the spectral-angular images, the roundness ratio R in the backward direction can be calculated using (3) as

$$R = \frac{|S_2|^2}{|S_1|^2} = \frac{\Delta I(\phi = 0^\circ)}{\Delta I(\phi = 90^\circ)}. \quad (5)$$

We estimated R averaged over λ from 400 to 700 nm for the control and AOM-treated colonic tissues in the distal segments. The average roundness ratio R for the AOM-treated colon tissues was found to be closer to 1 than one for the control colon tissues with one-tailed P-value = 0.021 as shown in Fig. 11(d). An increased average roundness of the subcellular structures in the precancerous epithelia may correlate with the partial loss of cell polarity and cell differentiation.

V. DISCUSSION

Our experiments show that the differential polarization signals (ΔI) are sensitive to the single scattering originating near the tissue surface. In the control colon tissues, the differential polarization signals (ΔI) show no Hb absorption in its spectra, although both the copolarized signals (I_{\parallel}) and the crosspolarized signals (I_{\perp}) contain the Hb absorption bands. The differential polarization signals (ΔI) are primarily contributed by the scatterers within the epithelia. The copolarized signals (I_{\parallel}) can be decomposed into the single scattering signals from the superficial tissues and the multiple scattering signals from the deeper tissues [21]. The crosspolarized signals (I_{\perp}) originate from the

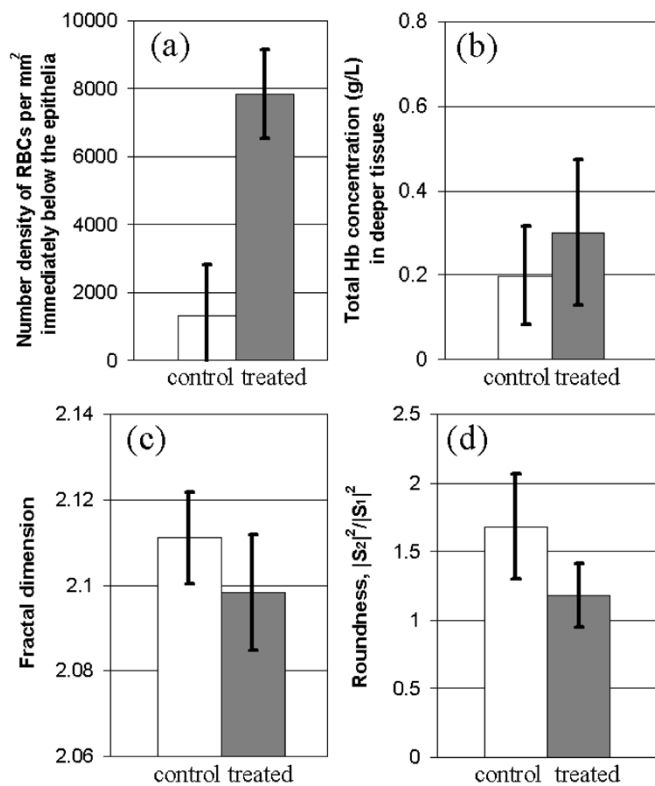


Fig. 11. Statistical analysis of the parameters characterizing tissue composition and microarchitecture. (a) The number density of RBCs in the capillary network underlying the epithelium, using the differential polarization signal (ΔI). (b) The Hb concentration (g/L) in deeper tissues, using the crosspolarization (I_{\perp}). The Hb concentrations in deeper tissues are not statistically different. (c) The fractal dimension of micro-structures in the epithelial microarchitecture from the analysis of the spectral-angular images. (d) The average roundness of subcellular structures in the epithelium. The error bars are the standard deviations.

deeper tissues, excluding the scattering from the upper tissues because the DOP of the incident light is highly maintained in the upper layers [16]. The multiple scattering signals contain the light scattered by collagen fibers in the connective tissues beneath the superficial tissues, as well as the spectral characteristics of the Hb absorption. The birefringence of the collagen fibers may rapidly depolarize the incident light, preserving the polarization of the incident light only in the superficial tissues [19], [20]. Thus, subtracting the crosspolarized signals from the copolarized signals ($\Delta I = I_{\parallel} - I_{\perp}$) is an effective method to restore the single scattering in the epithelia and to remove the diffused signal.

Our experiments with the AOM animal model demonstrate that light scattering can detect differences between normal and premalignant tissues at a very early stage of the disease, when no other morphological differences have been detected to date. To obtain the quantitative parameters differentiating the normal and precancerous tissues, we utilized the wealth of information provided by the multidimensional scattering intensity maps. The spectral, scattering angle, and azimuthal properties of light scattering were used in our analysis. The spectral distribution of the scattered light was used to measure the number density of RBCs in the capillary network underlying colonic epithelium. We found that the increased number densities of RBCs in

the precancerous tissues are highly statistically significant with $P = 0.0002$. This may indicate the change of the physiological requirements of the precancerous epithelial cells very early in the course of the disease. We point out that although an increase in blood supply by means of neovascularization has been well documented at the later stages of the carcinogenesis, our results present an evidence of changes in blood supply in the capillary network immediately underlying epithelia at the initial stages of the precancerous transformation [Fig. 11(a)]. Importantly, we found no significant changes in the Hb absorption in deeper subepithelial tissues [Fig. 11(b)]. These results confirm that, initially, only the blood supply to the epithelium is affected. We speculate that this increase in mucosal blood flow may be a consequence of the increase metabolic demands of these hyperproliferating premalignant colonocytes. It is well established in a variety of systems that autoregulatory ability in capillary systems can rapidly increase blood flow to metabolically active cells. This novel finding may have potential importance in our understanding of the early events in carcinogenesis.

The scattering angle distribution of the scattered intensity was used to estimate the fractal dimension D of tissue microarchitecture. We found that, on average, D is decreased in the AOM-treated tissues with $P = 0.033$, which may be indicative of the partial loss of correlation between the epithelial structures. Finally, the azimuthal sensitivity of our measurements was used to characterize the average roundness of subcellular structures. We found that the roundness ratio R increases in the precancerous tissues, thus indicating that, on average, the precancerous cells possess less polar structures. These results show that the microarchitecture of precancerous tissues is altered at the earliest stages of the colon-carcinogenesis. The loss of cell polarity and the disorganization of the epithelia in the early process of carcinogenesis have not been documented and investigated using the histopathology. Now, these alterations may be observed by means of light scattering.

Animal models are extremely valuable in understanding pathophysiologic mechanisms and developing treatment strategies for colon and other types of cancer. The AOM animal model has been widely used over the last decade to study colorectal carcinogenesis and the efficacy of various chemopreventive activities because of the similarities in histopathological, biochemical, molecular, and genetic defects with human colon cancer. In our experiments, we used this model to study the alterations of light-scattering signatures associated with the initial stages of precancer. Moreover, our finding is validated by the fact that these changes are observed in the regions of the rat colons where the AOM-induced carcinogenesis occurs, i.e., in the distal segment of the colon, and that no significant changes in light-scattering signatures were found in the proximal segments of the colons, where cancer does not typically develop. These evidences indicate that light-scattering signatures are altered due to carcinogenic effect of AOM rather than due to a nonspecific side effect of this agent. However, we note that animal studies cannot replace human clinical trials since no animal models can completely replicate the pathophysiology of a disease in all aspects. Thus, future human clinical studies are necessary to validate the light-scattering signatures.

Light scattering has several advantages over conventional methods of tissue diagnosis, for example, in histological analysis, the following apply. 1) The tissues can be studied in its natural state since tissue biopsy is not necessary and fixation and staining are not required. Conventional histology does not allow imaging living cells and requires using contrast agents. Light scattering provides information about the organization of living cells, which is not affected by artifacts, such as fixation or staining. This may result in the identification of previously undiscovered signatures of preinvasive cells. 2) The obtained information is quantitative. Microscopic analysis of cell morphology frequently concentrates on the visualization of specific structures, i.e., organelles, in particular cells. Light scattering does not attempt to visualize these structures, but provides *statistical* information about the structure of either individual cells or that of the population of as many as tens of thousands of cells. 3) The measurements can be performed in realtime, *in vivo*, or *in situ*. Therefore, the technique may facilitate high-throughput analysis as well as the studies of cellular changes associated with neoplastic transformations and anticancer therapies. 4) Light scattering can be used to guide biopsy, thus increasing the odds of identifying abnormal lesions and detecting diseased tissues that are not grossly visible with conventional methods. 5) Light scattering may be able to identify predysplastic changes, which may be reversible by treatment with chemopreventive agents. 6) Light scattering can complement other optical diagnostic techniques, such as fluorescence and diffuse reflectance spectroscopy. Studies have shown that such combinations, i.e., trimodal spectroscopy, improve the accuracy of the diagnosis [40]. Finally, we point out that although many features of scattering signals can be analyzed and translated into quantitative parameters characterizing tissue architecture, generally, information about multidimensional light-scattering signals is extremely rich and complicated. For example, certain minor features of the light-scattering signals from a cell organelle may depend not only on the size, shape, and internal organization of this organelle, but on the position of this organelle as part of a larger-scale structure, e.g., the cell itself, and the immediate surrounding of the organelle. Thus, the scattering signals contain the wealth of information awaiting new methods of analysis.

VI. CONCLUSION

We have developed an instrument, which enables obtaining the spectral, angular, azimuthal, and polarization dependence of light backscattering, offering the most comprehensive description of elastic light scattering. The experiments with the tissue phantoms showed that the single scattering and the multiple scattering can be effectively disentangled by means of the polarization gating, and that the scattering patterns in the spectral-angular images depend on the properties of scattering particles. In the studies with the rats with AOM treatment, we demonstrated that the analysis of the multidimensional scattering intensity maps enables obtaining quantitative information about tissue microarchitecture to detect the differences between the normal and premalignant tissues at a very early stage of the dis-

ease, when no other morphological differences have been identified by conventional histopathology. The spectral, scattering angle, and azimuthal properties of light scattering were used in our analysis to measure the number densities of the RBCs immediately below the epithelia, the fractal dimensions of the tissues, and the degree of roundness of subcellular structures, respectively. These parameters were found to be diagnostically significant for differentiating the precancerous and normal colonic tissues. The epithelial hyperemia in early carcinogenesis has potential significance as therapeutic targets as well. These results indicate that the microarchitecture of precancerous colonic tissues may be altered at the earliest stages of the disease. These alterations have not been described so far and may be further investigated by means of light scattering. Given the "field-effect" in colon carcinogenesis, this suggests that light scattering may have a role in clinical risk-stratification for more invasive procedures (i.e., colonoscopy).

ACKNOWLEDGMENT

The authors would like to thank Dr. R. J. Figueiredo and Dr. S. L. Jacques for valuable discussions and Dr. M. Bissonnette for experimental help.

REFERENCES

- [1] A. G. Yodh and B. Chance, "Spectroscopy and imaging with diffusing light," *Phys. Today*, vol. 48, pp. 34–40, 1995.
- [2] J. R. Mourant, I. J. Bigio, J. Boyer, R. L. Conn, T. Johnson, and T. Shimada, "Spectroscopic diagnosis of bladder cancer with elastic light scattering," *Laser Surg. Med.*, vol. 17, pp. 350–357, 1995.
- [3] S. K. Gayen and R. R. Alfano, "Sensing lesions in tissues with light," *Opt. Exp.*, vol. 4, pp. 475–480, 1999.
- [4] G. Zonios, L. T. Perelman, V. Backman, R. Manoharan, M. Fitzmaurice, J. Van Dam, and M. S. Feld, "Diffuse reflectance spectroscopy of human adenomatous colon polyps *in vivo*," *Appl. Opt.*, vol. 38, pp. 6628–6637, 1999.
- [5] K. Sokolov, R. A. Drezek, K. Gossage, and R. R. Richards-Kortum, "Reflectance spectroscopy with polarized light: Is it sensitive to cellular and nuclear morphology," *Opt. Exp.*, vol. 5, pp. 302–317, 1999.
- [6] I. J. Bigio, S. G. Bown, G. Briggs, C. Kelley, S. Lakhani, D. Pickard, P. M. Ripley, I. G. Rose, and C. Saunders, "Diagnosis of breast cancer using elastic-scattering spectroscopy: Preliminary clinical results," *J. Biomed. Opt.*, vol. 5, pp. 221–228, 2000.
- [7] A. E. Cerussi, D. Jakubowski, N. Shah, F. Bevilacqua, R. Lanning, A. J. Berger, D. Hsiang, J. Butler, R. F. Holcombe, and B. J. Tromberg, "Spectroscopy enhances the information content of optical mammography," *J. Biomed. Opt.*, vol. 7, pp. 60–71, 2002.
- [8] Y. L. Yang, E. J. Celmer, J. A. Koutcher, and R. R. Alfano, "DNA and protein changes caused by disease in human breast tissues probed by the Kubelka-Munk spectral function," *Photochem. Photobiol.*, vol. 75, pp. 627–632, 2002.
- [9] M. E. Brezinski and J. G. Fujimoto, "Optical coherence tomography: High-resolution imaging in nontransparent tissue," *IEEE J. Select. Topics Quantum Electron.*, vol. 5, pp. 1185–1192, July-Aug. 1999.
- [10] J. A. Izatt, M. D. Kulkarni, H. W. Wang, K. Kobayashi, and M. V. Sivak, "Optical coherence tomography and microscopy in gastrointestinal tissues," *IEEE J. Select. Topics Quantum Electron.*, vol. 2, pp. 1017–1028, Dec. 1996.
- [11] M. E. Zevallos, S. K. Gayen, B. B. Das, M. Alrubaiee, and R. R. Alfano, "Picosecond electronic time-gated imaging of bones in tissues," *IEEE J. Select. Topics Quantum Electron.*, vol. 5, pp. 916–922, July-Aug. 1999.
- [12] K. Chen, L. T. Perelman, Q. Zhang, R. R. Dasari, and M. S. Feld, "Optical computed tomography in a turbid medium using early arriving photons," *J. Biomed. Opt.*, vol. 5, pp. 144–154, 2000.
- [13] S. K. Gayen, M. Alrubaiee, H. E. Savage, S. P. Schantz, and R. R. Alfano, "Parotid gland tissues investigated by picosecond time-gated and optical spectroscopic imaging techniques," *IEEE J. Select. Topics Quantum Electron.*, vol. 7, pp. 906–911, Nov.-Dec. 2001.

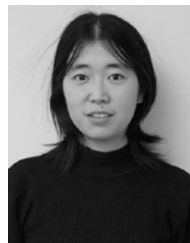
- [14] L. T. Perelman, V. Backman, M. Wallace, G. Zonios, R. Manoharan, A. Nusrat, S. Shields, M. Seiler, C. Lima, T. Hamano, I. Itzkan, J. Van Dam, J. M. Crawford, and M. S. Feld, "Observation of periodic fine structure in reflectance from biological tissue: a new technique for measuring nuclear size distribution," *Phys. Rev. Lett.*, vol. 80, pp. 627–630, 1998.
- [15] A. H. Hielscher, J. R. Mourant, and I. J. Bigio, "Influence of particle size and concentration on the diffuse backscattering of polarized light from tissue phantoms and biological cell suspensions," *Appl. Opt.*, vol. 37, pp. 125–135, 1997.
- [16] S. G. Demos, H. B. Radousky, and R. R. Alfano, "Deep subsurface imaging in tissues using spectral and polarization filtering," *Opt. Exp.*, vol. 7, pp. 23–28, 2000.
- [17] S. G. Demos and R. R. Alfano, "Optical polarization imaging," *Appl. Opt.*, vol. 36, pp. 150–155, 1997.
- [18] S. G. Demos, A. J. Papadopoulos, H. Savage, A. S. Heerdt, S. Schantz, and R. R. Alfano, "Polarization filter for biomedical tissue optical imaging," *Photochem. Photobiol.*, vol. 66, pp. 821–825, 1997.
- [19] S. L. Jacques, J. R. Roman, and K. Lee, "Imaging superficial tissues with polarized light," *Laser Surg. Med.*, vol. 26, pp. 119–129, 2000.
- [20] S. L. Jacques, J. C. Ramella-Roman, and K. Lee, "Imaging skin pathology with polarized light," *J. Biomed. Opt.*, vol. 7, pp. 329–340, 2002.
- [21] V. Backman, R. Gurjar, K. Badizadegan, R. Dasari, I. Itzkan, L. T. Perelman, and M. S. Feld, "Polarized light scattering spectroscopy for quantitative measurement of epithelial cellular structures in situ," *IEEE J. Select. Topics Quantum Electron.*, vol. 5, pp. 1019–1026, July-Aug. 1999.
- [22] V. Backman, L. T. Perelman, J. T. Arendt, R. Gurjar, M. G. Muller, Q. Zhang, G. Zonios, E. Kline, T. McGillican, T. Valdez, J. Van Dam, M. Wallace, K. Badizadegan, J. M. Crawford, M. Fitzmaurice, S. Kabani, H. S. Levin, M. Seiler, R. R. Dasari, I. Itzkan, and M. S. Feld, "Detection of preinvasive cancer cells in situ," *Nature*, vol. 406, pp. 35–36, 2000.
- [23] V. Backman, V. Gopal, M. Kalashnikov, K. Badizadegan, R. Gurjar, A. Wax, I. Georgakoudi, M. Mueller, C. W. Boone, R. R. Dasari, and M. S. Feld, "Measuring cellular structure at submicron scale with light scattering spectroscopy," *IEEE J. Select. Topics Quantum Electron.*, vol. 7, pp. 887–894, Nov.-Dec. 2001.
- [24] R. Gurjar, V. Backman, L. T. Perelman, I. Georgakoudi, K. Badizadegan, R. Dasari, I. Itzkan, and M. S. Feld, "Imaging of human epithelial properties with polarized light scattering spectroscopy," *Nature Med.*, vol. 7, pp. 1245–1248, 2001.
- [25] J. R. Mourant, T. M. Johnson, S. Carpenter, A. Guerra, T. Aida, and J. P. Freyer, "Polarized angular dependent spectroscopy of epithelial cells and epithelial cell nuclei to determine the size scale of scattering structures," *J. Biomed. Opt.*, vol. 7, pp. 378–387, 2002.
- [26] J. R. Mourant, J. P. Freyer, A. H. Hielscher, A. A. Eick, D. Shen, and T. M. Johnson, "Mechanisms of light scattering from biological cells relevant to noninvasive optical-tissue diagnostics," *Appl. Opt.*, vol. 37, pp. 3586–3593, 1998.
- [27] H. C. Van de Hulst, *Light Scattering by Small Particles*. New York: Dover, 1995.
- [28] R. G. Newton, *Scattering Theory of Waves and Particles*. New York: McGraw-Hill, 1969.
- [29] M. Kobaek-Larsen, I. Thorup, A. Diederichsen, C. Fenger, and M. R. Hoitinga, "Review of colorectal cancer and its metastases in rodent models: Comparative aspects with those in humans," *Comput. Med.*, vol. 50, pp. 16–26, 2000.
- [30] L. Roncucci, M. Pedroni, F. Vaccina, P. Benatti, L. Marzona, and A. De Pol, "Aberrant crypt foci in colorectal carcinogenesis. Cell and crypt dynamics," *Cell Prolif.*, vol. 33, pp. 1–18, 2000.
- [31] D. C. Chung, "The genetic basis of colorectal cancer: insights into critical pathways of tumorigenesis," *Gastroenterol.*, vol. 119, pp. 854–865, 2000.
- [32] R. K. Wali, S. Khare, M. Treiakova, G. Cohen, L. Nguyen, J. Hart, J. Wang, M. Wen, L. Joseph, A. Ramaswamy, M. Sitrin, T. Brasitus, and M. Bissonnette, "Ursodeoxycholic acid and F6-D3 inhibit aberrant crypt proliferation in the rat AOM model of colon cancer: roles of cyclin D1 and E-cadherin," *Cancer Epidemiol. Biomarkers Prev.*, vol. 11, pp. 1653–1662, 2002.
- [33] J. Folkman, "Tumor angiogenesis," in *The Molecular Basis of Cancer*, J. Mendelsohn, P. M. Howley, M. A. Ireal, and L. A. Liotta, Eds. Philadelphia, PA: Saunder, 1995, pp. 206–232.
- [34] J. M. Schmitt and G. Kumar, "Optical scattering properties of soft tissue: a discrete particle model," *Appl. Opt.*, vol. 37, pp. 2788–2797, 1998.
- [35] A. J. Einstein, H. S. Wu, and J. Gil, "Self-affinity and lacunarity of chromatin texture in benign and malignant breast epithelial cell nuclei," *Phys. Rev. Lett.*, vol. 80, pp. 397–400, 1998.

- [36] J. W. Baish and R. K. Jain, "Fractals and cancer," *Cancer Res.*, vol. 60, pp. 3683–3688, 2000.
- [37] J. Teixeira, "Experimental methods for studying fractal aggregates," in *On Growth and Form Fractal and Non-Fractal Patterns in Physics*, H. E. Stanley and N. Ostrowsky, Eds. Boston, MA: Martinus Nijhoff, 1986, pp. 145–162.
- [38] A. Wax, C. Yang, V. Backman, K. Badizadegan, C. W. Boone, R. R. Dasari, and M. S. Feld, "Cellular organization and substructure measured using single-resolved low-coherence interferometry," *Biophys. J.*, vol. 82, pp. 2256–2264, 2002.
- [39] J. B. A. Card and A. R. Jones, "An investigation of the potential of polarized light scattering for the characterization of irregular particles," *J. Phys. D: Appl. Phys.*, vol. 32, pp. 2467–2474, 1999.
- [40] I. Georgakoudi, V. Backman, E. Sheets, M. Muller, C. Crum, K. Badizadegan, M. Dasari, and M. S. Feld, "Diagnosis of cervical dysplasia with tri-modal spectroscopy," *Amer. J. Obstet. Gynaecol.*, vol. 186, pp. 374–382, 2002.



Young L. Kim received the B.S. degree in mechanical engineering from Hanyang University, Seoul, Korea, in 1997 and the M.S. degree in biomedical engineering, in 2002, from Northwestern University, Evanston, IL, where he is currently pursuing the Ph.D. degree in biomedical engineering.

His research interests include early cancer diagnosis and chemoprevention using light scattering, propagation of polarized light in biological tissues, and molecular imaging using nanoparticles.



Yang Liu received the B.S. degree in chemistry from Nankai University, Tianjin, China, in 1999 and M.S. degree in chemistry from the University of Chicago, Chicago, IL, in 2001. She is currently pursuing the Ph.D. degree in biomedical engineering at Northwestern University, Evanston, IL.

From 2001 to 2002, she was a Research Assistant at the University of Chicago, where she worked on the single molecule fluorescence spectroscopy. She joined the Biomedical Engineering Department, Northwestern University in 2002 and has been

working on the development of light-scattering instrumentation and the studies of the tissue light scattering for the early cancer diagnosis. Her current interest also includes development of novel molecular imaging techniques and theoretical studies of light scattering.

Ramesh K. Wali received the M.S. degree in biochemistry from Panjab University, Chandigarh, India, in 1980 and the Ph.D. degree in biochemistry from the India Institute Medical Education and Research, Chandigarh, India, in 1986.

He was a Postdoctoral Fellow in the Departments of Biochemistry and Medicine, University of Southern California, Los Angeles, from 1985 to 1987. Before joining Northwestern University, Evanston, IL, he was an Assistant Professor in the Section of Gastroenterology, Department of Medicine, University of Chicago, Chicago, IL. Currently, he is a Research Associate Professor in the Department of Medicine, Evanston–Northwestern Healthcare/Northwestern University, Evanston, IL.



Hemant K. Roy received the B.S. degree (*summa cum laude*) in molecular biology from Vanderbilt University, Nashville, TN, in 1985 and the M.D. degree with distinction from Northwestern University, Evanston, IL, in 1989. He completed his internal medicine training at Beth Israel Hospital/Harvard Medical School, Cambridge, MA, in 1992 and gastroenterology training at the University of Chicago, Chicago, IL, from 1992 to 1995.

He was an Assistant Professor of medicine at University of Nebraska Medical Center/Eppley Cancer Institute, Omaha, from 1995 to 2002. Currently, he is an Associate Professor of medicine at Evanston Northwestern Healthcare/Northwestern University. His primary clinical and research interests are on early detection and chemoprevention of colorectal cancer.



Michael J. Goldberg received the M.D. degree from the University of Illinois, Chicago, where he also completed his residency. He completed his Fellowship at Tufts New England Medical Center, Medford, MA.

He is the Head of the Division of Gastroenterology, Evanston Northwestern Healthcare, Evanston, IL, specializing in gastroenterology and hepatology. Currently, he is an Associate Professor at the Feinberg School of Medicine, Northwestern University, Evanston, IL. Since joining the GI

Division in 1999, he has significantly expanded the division's clinical research and education components. Previously, he was the Director of Therapeutic Endoscopy at the University of Chicago Hospital, Chicago, IL, as well as the Chief of Gastroenterology at Weiss Memorial Hospital, Chicago, IL. His main area of interest is pancreaticobiliary tract disease and colon cancer prevention and detection.



Kun Chen received the B.S. and M.S. degrees in physics from the University of Science and Technology of China, Hefei, China, in 1991 and 1993, respectively, and the Ph.D. degree in physics from Massachusetts Institute of Technology, Cambridge, MA, in 2000.

His research interests include photon migration in turbid media, time-domain optical computerized tomography, development of biomedical devices, and optical spectroscopy and imaging techniques for cancer diagnosis.



Alexey K. Kromin received the M.S. degree in thermophysics and optics from St. Petersburg University of Fine Mechanics and Optics, St. Petersburg, Russia, in 1988.

He joined a research branch of the Laser Technologies Department, St. Petersburg University of Fine Mechanics and Optics as a Research Engineer. He became a Research Fellow, Senior Research Fellow, and Head of the Education Laboratory of the Laser Technologies Department. He was invited to join a team of scientists at the Center for Quality Engineering,

Northwestern University, Evanston, IL, in 1997 as a Visiting Scholar and later worked as a Research Engineer in the field of laser-based ultrasonics and fiber optic sensor design. Since 2002, he has been working as a Research Engineer in the Biomedical Engineering Department, Northwestern University. His current research interests are in the field of design and applications of fiber optics devices for light scattering spectroscopy.



Vadim Backman received the M.S. degree from St. Petersburg Technical University, St. Petersburg, Russia, in 1996, the M.S. degree in physics from the Massachusetts Institute of Technology, Cambridge, in 1998, and the Ph.D. degree in medical engineering and medical physics from Harvard University and the Massachusetts Institute of Technology, Cambridge, in 2001.

He is an Assistant Professor of biomedical engineering at Northwestern University, Evanston, IL. His research interests include biomedical optics, spectroscopy, development of theoretical approaches to describe light propagation in biological media, and optical diagnostic imaging.